Eur. Phys. J. C (2025) 85:84
https://doi.org/10.1140/epjc/s10052-025-13823-9

THE EUROPEAN PHYSICAL JOURNAL C

Regular Article - Experimental Physics

QCD predictions for simultaneously produced Higgs and vector bosons at $\sqrt{s}$ = 13, 14, 27 and 100 TeV with a comprehensive study of systematic uncertainty and charge asymmetry

Kamuran Dilsiz[1,2,a], **Emrah Tiras**[2,3,b], **Meryem Yilmaz**[1,c], **Hasan Ogul**[4,d]

[1] Department of Physics, Faculty of Art and Science, Bingol University, 12000 Bingol, Turkey
[2] Department of Physics and Astronomy, The University of Iowa, Iowa City, IA 52241, USA
[3] Department of Physics, Faculty of Science, Erciyes University, 38030 Kayseri, Turkey
[4] Department of Nuclear Engineering, Faculty of Engineering and Architecture, Sinop University, 57000 Sinop, Turkey

Received: 30 June 2024 / Accepted: 16 January 2025

Abstract A comprehensive study of high-order QCD cross-section for the Higgs boson that is simultaneously produced with a vector boson is presented at $\sqrt{s}$ = 13, 14, 27 and 100 TeV in this manuscript. The simultaneous Higgs production with a vector boson facilitates the investigation of the Higgs signal. In the calculations, three different branching states of the Higgs ($\tau^-\tau^+$, $b\bar{b}$, $\gamma\gamma$) and vector bosons [$W^{\pm}(e^{\pm}\nu(\bar{\nu}))$, $Z(e^-e^+)$] were taken into account. Here, leading order (LO), next-to-leading order (NLO), and next-to-NLO (NNLO) QCD cross-sections were calculated for these branching states. A simulation framework was built for the calculations at the TRUBA high-performance grid computing center. Then, the threshold values (selection cuts) close to the values used by the CMS and ATLAS Collaborations were selected and used on several parameters such as invariant mass, transverse momentum (p_T), pseudorapidity (η), etc. In addition, NNPDF3.1 parton distribution functions (PDF) were used during the calculation. The results showed that the numerical value of the QCD prediction increases at NLO and NNLO as compared to the LO predictions. In addition to the higher-orders, the cross-section value increases as the center-of-mass energy increases. In addition to the QCD predictions, PDF, scale, and α_S uncertainties of the QCD predictions were also calculated to test the reliability of the high-order QCDs. The results showed that total and scale uncertainties decrease as the QCD order increases. In addition, it was found that LO total and scale uncertainties increase significantly as the center-of-mass energy increases, while NLO and NNLO scale and total uncertainties remain almost constant or show a negligible increase as the center-of-mass energy increases. This indicates that high-order QCDs not only provide more accurate results by the addition of extra partonic diagrams but also provide lower uncertainties in the relevant production channels. Furthermore, the required data that provides the exact statistics for physics measurements of simultaneously produced Higgs and vector bosons as the data at 13 TeV were predicted at $\sqrt{s}$ = 14, 27, and 100 TeV. As a result, we found that the same statistics for accurate physics measurements can be obtained at $\sqrt{s}$ = 14, 27, and 100 TeV with approximately 1.1, 2.0, and 6.5 times less data than the amount of data at $\sqrt{s}$ = 13 TeV, respectively. In the last section of this study, W boson charge asymmetry was computed at NNLO QCD. The lowest charge asymmetry between W^+ and W^- was obtained at the WH($\tau^-\tau^+$) decay channel and the highest charge asymmetry results were obtained at the WH($b\bar{b}$) decay channel.

1 Introduction

There has been an enormous effort by experimental physicists to prove the existence of the Higgs boson since it was theorized in the 1960s. A search for the SM Higgs boson was previously conducted at the Tevatron accelerator [1], but no evidence was found. The large hadron collider (LHC), which has almost ten times higher center-of-mass energy than Tevatron's was established at CERN with the main goal of searching for the existence of the Higgs boson. At the LHC, the first proton beams were smashed at 7 TeV in 2010 and

[a] e-mail: kdilsiz@bingol.edu.tr (corresponding author)
[b] e-mail: etiras@fnal.gov
[c] e-mail: meryyilmz@gmail.com
[d] e-mail: hogul@sinop.edu.tr

the center-of-mass energy ($\sqrt{s}$) was increased to 8 TeV after two years. The CMS and ATLAS Collaborations carefully analyzed the data recorded at these energies and the discovery of a new boson (Higgs) with a mass of 125 GeV was announced in 2012 [2,3]. Following this important discovery, studies on the Higgs boson intensified and many physics analyses were conducted on different production channels of the Higgs boson [4–19].

Currently, the LHC is running at 13.6 TeV center-of-mass energy, and the high luminosity LHC (HL-LHC) is scheduled to begin operations in late 2027 at a center-of-mass energy of 14 TeV with an integrated luminosity approximately ten times more intense than the LHC [20]. Thus, better results in various previous analyses are planned to be obtained with the increased luminosity. In addition to the analyses about the SM Higgs boson at the HL-LHC, the analyses in the beyond-SM (BSM) such as the analysis of the Higgs boson in electroweak symmetry breaking scenarios [21] are also planned to be implemented.

The future circular collider (FCC) is a high-energy hadron collider planned to be built at CERN in the future to achieve integrated luminosities and energies beyond what the LHC and HL-LHC can achieve. This will provide an opportunity to test physics theories that could not be tested at the LHC level energies. The FCC will not be limited to proton or ion collisions as in the LHC, but it will also allow electron–positron collisions. In this context, FCC will have three separate accelerators: electron–positron, high energy LHC (HE-LHC), and FCC-hh (proton–proton, ion–ion). HE-LHC is planned to be located in the same tunnel as the LHC and the proton beams are planned to be collided with a center-of-mass energy of 27 TeV [22]. FCC-hh is planned to be operated in a 100 km tunnel in circumference and the proton beams at FCC will collide with a center-of-mass energy of 100 TeV. This will provide a total integrated luminosity of 20 ab^{-1} and produce approximately 10^{10} Higgs events [23].

One of the potential decay channels of the SM Higgs boson is a bottom (b) quark and an anti-bottom ($\bar{b}$) quark pair [24–27]. This decay process leads to significant background events arising from multi-jet production. To overcome this background, a more sensitive production channel of the Higgs boson should be tested. The simultaneous production of the Higgs boson with a vector boson is one of these sensitive methods since it provides background-signal separation by reducing the background resulting from multi-jet events.

In hadronic collisions, the cross-section value increases as the center-of-mass energy increases because higher center-of-mass energies result in more events than the number of events at lower center-of-mass energies. Hence, higher center-of-mass energy events provide a more sensitive measurement for the Higgs and simultaneous processes with Higgs. In the previous studies, the value of the mass of the SM Higgs boson was calculated using the production channels of Higgs decaying to gamma pair ($H \rightarrow \gamma\gamma$) and leptons ($H \rightarrow 4l$) [4]. These analyses include statistical and systematic uncertainties and individual mass measurements of each production channel. Analysis of the SM predictions and the deviations in the SM due to the BSM processes can be done through the channel that Higgs decays into a gamma pair. In this respect, the study of Higgs boson decays into gamma pair is more crucial among the other decay channels of the Higgs boson. Moreover, the $H \rightarrow \gamma\gamma$ study is one of the most critical studies on the discovery of Higgs since analyzing the Higgs decays into gamma pair provides a clean signal in which background is suppressed.

Previously, CMS and ATLAS collaborations published the results of comprehensive analysis on $H \rightarrow \gamma\gamma$ channel with 13 TeV LHC Run 2 data [7,28]. In addition to $b\bar{b}$ and $\gamma\gamma$ channels, $H \rightarrow 4l$ channel is also vital in the Higgs analysis because it has a large signal/background ratio and a narrow resonance width [29]. Because of their importance in the Higgs studies, decay channels of WH and ZH are selected as W and Z decay into the leptons, and Higgs decays into $b\bar{b}$, $\gamma\gamma$ and $\tau^+\tau^-$.

A comprehensive report including simulation and theoretical studies towards the experiments planned to be established at CERN was published in 2018 [30–34]. In the first part of the report, the aims of the HL-LHC for strong, weak, and electromagnetic interactions were detailed and the HL-LHC potential to be upgraded to HE-LHC was discussed [30]. The WH and ZH production channels were mentioned in the second part of the report [31], which is discussed in detail in the next paragraph. While the third part of the report [32] gives a detailed study of the physics analyses for the SM and BSM, it does not include a study of the FCC. The studies at [33] include analyses of flavor physics and the studies at [34] include analyses of Quark Gluon Plasma (QGP).

The second part of the report mentioned the results of a study conducted in 2003 on the NLO QCD and electroweak production of W and Z bosons and the Higgs boson at the LHC and Tevatron experiments [35]. In this study, the cross-sections of the Higgs boson were calculated at 1.96 TeV and 14 TeV energies without including the branching fractions of the Higgs boson into leptons or quarks. In addition, the cross-section of the simultaneous production of the Higgs boson with a vector boson was calculated up to the NNLO order at energies of 1.96 TeV and 14 TeV in 2004 [36]. In this referred study, the highest QCD level (NNLO) was calculated at 14 TeV but the branching fractions of the Higgs and vector bosons, and the calculations at the FCC energies are missing.

Later, in two separate studies conducted between 2012 and 2015, Higgs Strahlung and vector boson fusion Higgs (VBFH) processes were calculated up to the NLO order using the HAWK program [37,38]. Considering the different mass values of the Higgs boson (115–130 GeV), cross-section calculations up to the NLO order were made in 2013 for the production channels $pp \rightarrow WH$ and $pp \rightarrow ZH$ at the center-of-mass energies of 8 and 14 TeV [39]. In addition, the cross-sections of the simultaneously produced Z and Higgs bosons as a result of gluon–gluon fusion, were calculated based on the center-of-mass energies of the LHC up to the next-to-leading logarithmic (NLL) correction [40]. Moreover, studies including SM and BSM gluon–gluon fusion and $b\bar{b}$ to WH and ZH processes were conducted in 2018 [41]. However, these studies do not include the NNLO order and FCC energies. In addition, the study at [40] includes only the $gg \rightarrow ZH$ production process and does not include quark processes that contribute to ZH production. Another study of WH and ZH with the effect of top quark loops on the Higgs generation at $\sqrt{s}$ = 14 TeV was previously carried out to investigate the effect of high order corrections on the relevant channels [42]. Moreover, QCD radiative corrections to the SM Higgs boson associated with a W boson were performed at the high p_T region. Here, a fully differential computation that include W boson decay products was presented and the work presented the effect of higher order corrections on the kinematic distributions [43]. A fully differential NNLO QCD calculation for the ZH channel can be found at [44]. The study provides NNLO QCD at $\sqrt{s}$= 8 and 14 TeV, and highlights the significance of loop-induced gluon–gluon fusion processes and their contributions to the overall production cross-section as well as the transverse-momentum distribution. Because of this, our study comprehensively includes both gluon–gluon processes and quark-quark interactions as well as $\sqrt{s}$= 27 and 100 TeV energies, which are not studied in the studies mentioned above.

In this study, we calculated QCD predictions of nine production channels of WH and ZH production processes including systematic uncertainties and charge asymmetry of W^+ and W^- at 13, 14, 27, and 100 TeV center-of-mass energies for the first time. The results of these calculations provide scientists in the field with an early assessment of the expected performance of upcoming high-energy accelerators such as the HL-LHC, HE-LHC, and FCC. The computations of QCD cross-sections were simulated focusing on several parameters such as transverse momentum (pT), invariant mass, pseudorapidity (η), and so on. These calculations apply to the decay of a lepton or a quark within a chosen production channel. This analysis also enables the investigation of the impact of the channel on the kinematic distributions by applying different selection cuts. Calculating high-order QCD cross-sections with this computational method at the energy levels of HL-LHC (14 TeV), HE-LHC (27 TeV), and FCC-hh (100 TeV) will enhance the detection of the Higgs signal.

2 Material and methods

In hadronic collisions, the cross-section defines the probability of the particles occurring or interacting in a certain way. There are multiple cases in which a particle occurs or interacts in high-energy collisions. Because of this, extra particle interaction diagrams need to be taken into account while calculating the cross-section. Compared to the initial particle interaction diagram, each extra diagram may have different amplitudes which may cause different cross-section values to be obtained. Beyond the LO prediction, the extra diagrams involved in the process result in higher-order predictions such as NLO and NNLO QCD. The cross-section of higher-order predictions cannot be calculated using perturbation theory, which allows direct scattering calculation. However, if the cross-section is reduced to a partonic cross-section, it can be calculated in perturbative QCD (pQCD). Equation 1 shows that the cross-section of a particle is calculated using partonic cross-section and parton distribution functions (PDFs).

$$\sigma_{pp\rightarrow X} = \sum_{a,b} \int_0^1 dx_a \int_0^1 dx_b f_a(x_a, \mu_F) f_b(x_b, \mu_F) \times \hat{\sigma}_{ab\rightarrow X}(x_a P_A, x_b P_B, \mu_F, \mu_R) \tag{1}$$

where X is the particle that occurs in a pp collision, $f_{ab}(x_a x_b, \mu_F)$ is PDF, x_a and x_b are the fractions of incoming hadron's momentum, $\hat{\sigma}_{ab\rightarrow X}(x_a P_A, x_b P_B, \mu_F, \mu_R)$ is the partonic cross-section, a and b are the subatomic particles such as quarks and gluons that occur in a pp collision, P_A and P_B are the momentum of incoming protons. More details about this equation can be found in Ref. [45]. The partonic cross-section given in Eq. (1) can be calculated using the power series of the strong coupling constant (α_S) as shown in Eq. (2). This shows that each α_S power corresponds to the contributions from higher-order diagrams.

$$\hat{\sigma}_{ab\rightarrow X} = [\hat{\sigma}_{LO} + \alpha_S \hat{\sigma}_{NLO} + \alpha_S^2 \hat{\sigma}_{NNLO} + \cdots] \tag{2}$$

After a pp collision occurs, the valance quarks in a proton behave like free quarks and move away from each other (asymptotic freedom) until their distance reaches approximately the diameter of a hadron (10^{-15} m). Then, new quark-gluon pairs called partons are formed because of the increasing energy between the quarks. PDFs provide the probability that these new particles carry a certain fraction of the total momentum of hadrons. So, they are necessary parameters to calculate cross-section in inelastic pp collisions.

Table 1 Different selections used in the calculation of the scale uncertainty

(μ_R, μ_F)	
(1,1)	$\mu_R = \mu_F = M_{VH}$
(1, 2)	$\mu_R = M_{VH}, \mu_F = 2M_{VH}$
(1, 1/2)	$\mu_R = M_{VH}, \mu_F = 1/2M_{VH}$
(2, 1)	$\mu_R = 2M_{VH}, \mu_F = M_{VH}$
(2, 2)	$\mu_R = \mu_F = 2M_{VH}$
(2, 1/2)	$\mu_R = 2M_{VH}, \mu_F = 1/2M_{VH}$
(1/2, 1)	$\mu_R = 1/2M_{VH}, \mu_F = M_{VH}$
(1/2,2)	$\mu_R = 1/2M_{VH}, \mu_F = 2M_{VH}$
(1/2, 1/2)	$\mu_R = \mu_F = 1/2M_{VH}$

Table 2 Decay channels

$pp \to W^+ + H$
$[W^+ \to \nu + e^+] + [H \to \gamma\gamma]$
$[W^+ \to \nu + e^+] + [H \to b\bar{b}]$
$[W^+ \to \nu + e^+] + [H \to \tau^+\tau-]$
$pp \to W^- + H$
$[W^- \to \bar{\nu} + e^-] + [H \to \gamma\gamma]$
$[W^- \to \bar{\nu} + e^-] + [H \to b\bar{b}]$
$[W^- \to \bar{\nu} + e^-] + [H \to \tau^+\tau-]$
$pp \to Z + H$
$[Z \to e^- + e^+] + [H \to \gamma\gamma]$
$[Z \to e^- + e^+] + [H \to b\bar{b}]$
$[Z \to e^- + e^+] + [H \to \tau^+\tau-]$

The cross-sections in this study were computed by using the MCFM program [46] and LHAPDF library' [47] which also implements Eqs. (1) and (2). During the simulation, NNPDF3.1 [48] with the PDF dataset containing 100 different datasets was used.

The amplitude of a diagram for the particle interactions can be obtained using Feynman calculations and the cross-section value is proportional to the square of this amplitude. However, the amplitude is influenced by two types of divergences; infrared (IR) and ultraviolet (UV) in perturbative QCD (pQCD) [49]. The factorization scale (μ_F), which is a function of PDFs, is used to repair IR divergences caused by low-energy gluons. The renormalization factor (μ_R), a function of a strong coupling constant, is used to repair UV divergences caused by large momentum in the loops of Feynman diagrams. In the standard method for the calculation of the scale uncertainty, μ_F and μ_R are initially fixed to the sum of the masses of the Higgs and W/Z bosons to correct the mentioned IR and UV divergences and calculate the accurate cross-section. The cross-section calculations are repeated by taking twice and half of the μ_R and μ_F to obtain the scale uncertainties that are calculated using Eqs. (3) and (4). In addition to the standard convention, the values of μ_R and μ_F must be varied independently to find more accurate results for the scale uncertainty. Table 1 lists the different variations of μ_R and μ_F that were used for the calculation of the scale uncertainty.

In this study, similar to the standard method, the default value of μ_R and μ_F were initially fixed to the sum of the masses of the Higgs and vector (W and Z) bosons. Then, LO, NLO, and NNLO predictions were calculated for all production channels given in Table 2. To obtain the scale uncertainties, the cross-section calculations were repeated by varying μ_R and μ_F independently in between $1/2M_{VH} \leq \mu_R, \mu_F \leq 2M_{VH}$. The scale uncertainty for each selection was calculated using Eq. (5) and the final scale uncertainty was selected as the highest value among the calculated results.

Similarly, the initial α_S value was taken as 0.118, and α_S uncertainties were calculated changing the α_S value to 0.116 and 0.120, as shown in Eqs. (6) and (7).

$$\Delta Scale^+ = |Scale1 - Scale2| \quad (3)$$

$$\Delta Scale^- = |Scale1 - Scale3| \quad (4)$$

where Scale1, Scale2, and Scale3 are the QCD results obtained by the sum, twice, and half of the total masses of the Higgs and vector bosons, respectively.

$$\Delta Scale^\pm = |Scale1 - Scale4| \quad (5)$$

where Scale1 is the QCD results obtained by the sum of the total masses of the Higgs and vector bosons, Table 1 (1,1), and the Scale4 is the QCD results obtained by other variations of (μ_R, μ_F). Among these results the highest $\Delta Scale^\pm$ was selected as scale uncertainty.

$$\alpha_S^+ = |\alpha_{S_1} - \alpha_{S_2}| \quad (6)$$

$$\alpha_S^- = |\alpha_{S_1} - \alpha_{S_3}| \quad (7)$$

where α_{S_1}, α_{S_2} and α_{S_3} are the QCD results obtained by $\alpha_S = 0.118, 0.116$ and 0.120, respectively.

This study is dedicated to providing preliminary results of the simultaneous production of Higgs and vector bosons for future high-energy experiments such as the HE-LHC and FCC. To obtain accurate results and reduce the background events, it is vital to apply threshold requirements carefully on the parameters such as p_T, η, etc. So, all the selection cuts on different parameters applied throughout this study were given in Table 3. These selection cuts are similar threshold values with the ones used by the CMS and ATLAS experiments for WH and ZH studies at $\sqrt{S}$ = 13 TeV [50–52]. However, the same threshold cuts of CMS and ATLAS were not exactly applied on the leptons and jets in the final state. CMS and ATLAS collaborations used different selection cuts on the

Table 3 Applied selections. "j" is equivalent to b, τ, γ or their anti-particles

$p_T^j > 30$ GeV
$\mu_R = \mu_F = M_H + M_{W/Z}$
$p_T^l > 20$ GeV
$\lvert\eta_l\rvert < 2.4$, $\lvert\eta_j\rvert < 2.4$
$\alpha_s = 0.118$
75 GeV$< M_Z <$105 GeV
$m_t = 173.2$ GeV, $m_c = 1.275$ GeV and $m_b = 4.66$ GeV

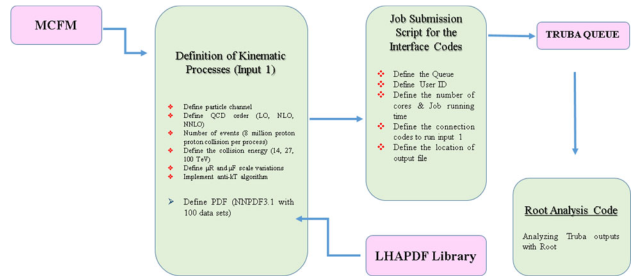

Fig. 1 The operational mechanism of the simulation codes

first and second leptons and jets in their final state. In contrast, we used the same cuts on both electrons ($p_T^{e1} > 20$ GeV and $p_T^{e2} > 20$ GeV) and jets (p_T^b, p_T^τ and $p_T^\gamma > 30$ GeV) in our final state. We considered the production and decay processes as a single (coherent) process to calculate the full matrix element for the entire process. Having two leptons and two jets ($b\bar{b}$, $\tau^-\tau^+$ and $\gamma\gamma$) in the final state, we calculated the entire process including all interferences and correlations between production and decay channels. This method provides more accurate results as it reduces the possibility of interference effects caused by the decay products that may arise from different interactions. Because of the higher-order corrections and interference effects, the final cross-section results calculated coherently might be different than the cross-section results that are factorized with branching ratios. Even though coherent calculations are more complex and complicated for the computational processes, the results of coherent calculations are more accurate and compatible with the experimental results. In this study, the definition of jets is made with the anti-k_T algorithm [53] which defines the particles based on their spatial distance in the η-ϕ plane. The input parameter used in the MCFM program defines the decay process of the particles that are created after the pp collision. This parameter initially defines if the particle from Higgs decay would be b quarks, gamma, or tau pairs. If the final state of the selected process contains quarks, gluons, gammas, or taus, every event will involve an attempt to generate these particles into jets. Therefore, the jets created in the final state are separated by ΔR jet cut which is defined by the quadratic sum of the $\Delta\eta$ and $\Delta\phi$. In this analysis, we used $\Delta R > 0.5$ to separate jets.

To compute the QCD cross sections, the TRUBA clusters provided by the Scientific and Technological Research Council of Türkiye (TÜBİTAK) ULAKBİM Grid computing center were used. The TRUBA clusters are intended to handle a broad variety of computational jobs in different scientific domains. The system consists of multiple specialized nodes such as multi-core CPU nodes for general-purpose computing, memory-optimized nodes with large RAM capacities for data-intensive applications, and GPU nodes that utilize powerful graphical processing units for parallel processing tasks and they are perfect for simulations and machine learning studies. Large datasets are accessed quickly with the cluster's high-performance storage, and effective data transfer is ensured by high-speed networking. TRUBA uses an organized queue system to make job submissions easier. Researchers can submit jobs in the TRUBA clusters based on their requirements. We specifically used standard queues, long and short queues. Among these queues, the standard queue serves as the main queue for general jobs and offers a well-balanced strategy for different types of workloads. The long queue is designed for jobs requiring longer runtimes such as NNLO QCD processes. The complex computations are performed faster with the help of the long queue. The maximum run time for both standard and long queues is 15 days for each job. The short queue has a maximum run time of four hours and is designed for short operations such as LO QCD calculations. In addition to these queues, the Interactive queue enables users to run and debug their programs interactively. The GPU queue is only used for jobs that require GPU resources. It is the best-suited queue for parallel processing activities, especially in data visualization and machine learning analysis.

The selection cuts on the parameters defined and calculations were implemented in the simulation code using the following steps:

(1) The MCFM Monte Carlo program and datasets containing PDFs in the LHAPDF library were installed in the TRUBA cluster, which is the TÜBİTAK ULAKBİM Grid computing center, and scripts were developed to provide an interface to run these two programs together. Figure 1 shows how these calculations are transferred to the simulation code. A set of simulation codes involving kinematic processes such as QCD orders, energies, μ_R and μ_F, anti-k_T algorithm, and PDFs integration with the MCFM program were defined as shown in the figure.

(2) An interface package that compiled the MCFM program and LHAPDF together was created and included the user ID of each user, the TRUBA queue to which the simulation code is transferred, and the name of the particle channel in which the QCD cross-section is calculated.

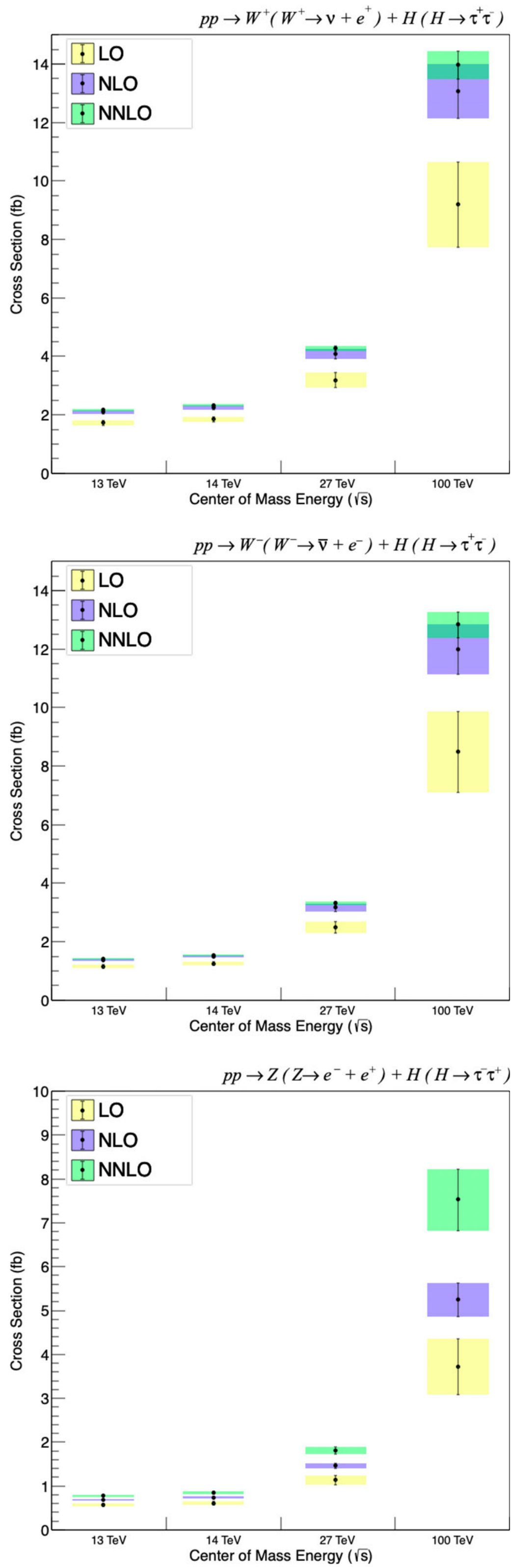

Fig. 2 The comparison of LO, NLO, and NNLO QCD cross-sections that are calculated at $\sqrt{s}$= 13, 14, 27 and 100 TeV for W^+H (top), W^-H (middle), ZH (bottom) channels. In these channels, the Higgs boson decays to a pair of tau leptons, and vector bosons decay to electrons and their neutrino flavors

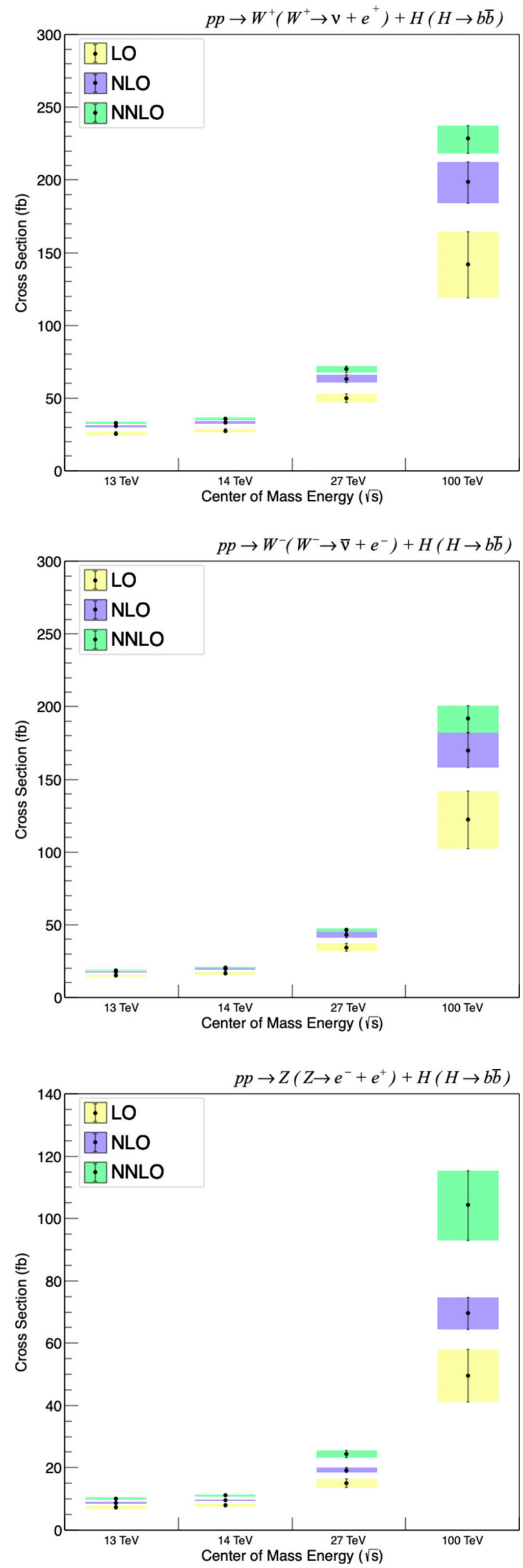

Fig. 3 The comparison of LO, NLO and NNLO QCD cross-sections calculated at $\sqrt{s}$= 13, 14, 27 and 100 TeV for W^+H (top), W^-H (middle), ZH (bottom) channels. In these channels Higgs boson decays a pair of b quarks and vector bosons decay to electrons and their neutrino flavors

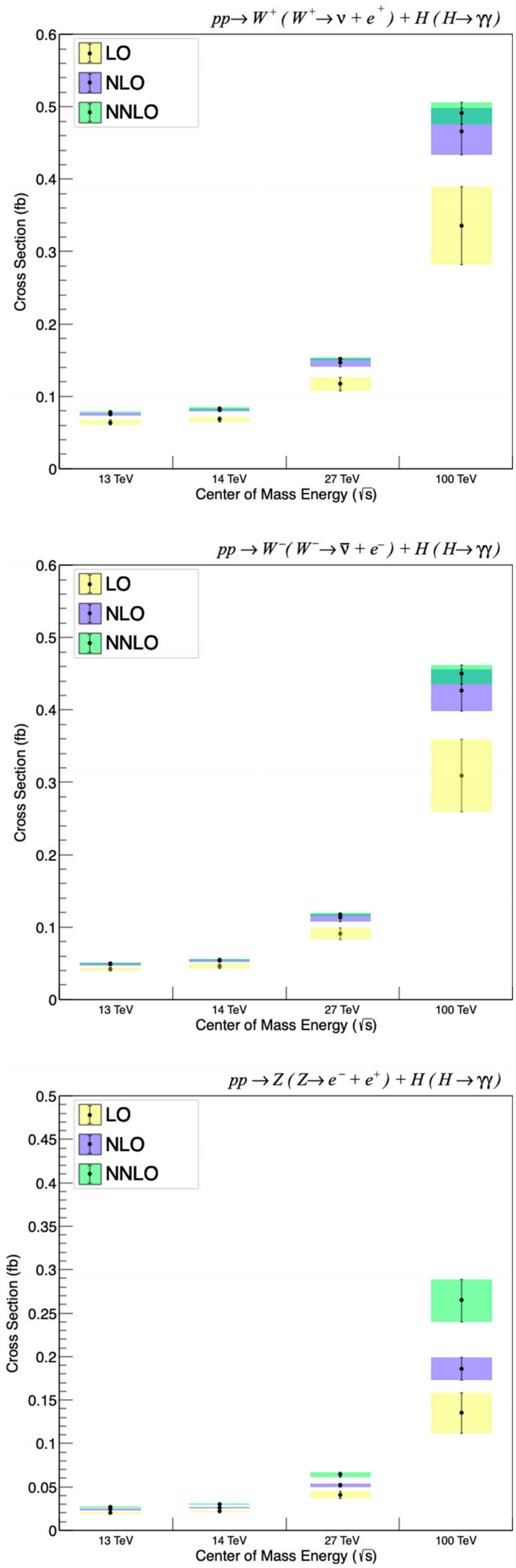

Fig. 4 The comparison of LO, NLO and NNLO QCD cross-sections calculated at $\sqrt{s}$= 13,14, 27 and 100 TeV for W^+H (top), W^-H (middle), ZH (bottom) channels. In these channels Higgs boson decays a pair of gamma and vector bosons decay to electrons and their neutrino flavors

(3) To obtain more accurate results, the number of collisions was increased to eight million events for each process. The jobs were directed to TRUBA queues to run on high-core PCs for a shorter processing time as defined in Fig. 1.

(4) After an average of 8–10 days, the jobs directed to TRUBA queues were completed and the results were copied to our local machines. The final results were analyzed on the local machine using the Root analysis program.

Finally, the data requirements for the same production channels at 14, 27, and 100 TeV energies were calculated using the obtained QCD cross-sections and compared with the data received at 13 TeV energy. In the calculations, NNLO QCD corrections were first considered to match the experimental data, and the relationship between the cross-section and the event count with luminosity (N = σxL) was utilized. This method determined the amount of data required to obtain experimental statistics at higher energies, such as 14, 27, and 100 TeV, based on the data obtained at 13 TeV energy.

3 Results and discussions

This study aims to calculate the QCD predictions for Higgs boson (H) and vector bosons (W and Z) produced concurrently for the LHC and potential future high-energy colliders. The calculation method includes a simulation study that carries high-order QCD predictions of many branching states of Higgs boson and vector bosons. This method comprises a series of simulation interface codes that enable the integration of the MCFM program installed in the TRUBA high-performance grid computing center and the LHAPDF library. All the jobs of the simulation were run through TRUBA queues on the high-core PCs. In the scope of this study, three different channels were simulated for both WH and ZH production channels and their QCD predictions were calculated at $\sqrt{s}$ = 13, 14, 27 and 100 TeV.

Figures 2, 3 and 4 show the comparison of LO, NLO, and NNLO QCD predictions that are calculated at 13, 14, 27, and 100 TeV center-of-mass energies for the simultaneous production of Higgs and vector bosons. In all the figures, W^+ decays to $e^+\nu$, W^- decays to $e^-\bar{\nu}$ and Z decays to e^-e^+. Meanwhile, H decays to $\tau^-\tau^+$, $b\bar{b}$ and γ pair in the Figs. 2, 3 and 4, respectively.

In the figures, the cross-section increases at higher QCD orders and as the center-of-mass energy increases. The sizes of the intervals in yellow, blue, and green colors show the total uncertainties for LO, NLO, and NNLO calculations, respectively. The change in the QCD shape is low at NLO and NNLO predictions as compared to LO predictions in all energy ranges.

Tables 4, 5 and 6 show the numerical results for the QCD predictions at $\sqrt{s}$ = 13, 14, 27 and 100 TeV for the production channels W^+H, W^-H and ZH, where vector bosons

Table 4 LO, NLO and NNLO QCD predictions for the channels of W^+H, W^-H and ZH at $\sqrt{s} = 13$, 14, 27 and 100 TeV. For all channels W^+ decays to $e^+\nu$, W^- decays to $e^-\bar{\nu}$, Z decays to e^-e^+, H decays to $\tau^-\tau^+$ and all units are in fb. The uncertainties were calculated taking the quadratic sum of the PDF, scale and α_S, and provided as the percentage (±%) of the QCD results

		13 TeV	14 TeV	27 TeV	100 TeV
W^+H	LO	$1.731^{+4.326}_{-4.778}$	$1.847^{+4.564}_{-4.997}$	$3.187^{+7.242}_{-7.923}$	$9.190^{+15.805}_{-15.918}$
	NLO	$2.094^{+1.800}_{-1.576}$	$2.246^{+1.696}_{-1.545}$	$4.092^{+1.469}_{-1.408}$	$13.060^{+2.698}_{-2.987}$
	NNLO	$2.170^{+1.894}_{-1.461}$	$2.333^{+1.616}_{-1.509}$	$4.280^{+1.416}_{-1.390}$	$13.978^{+1.281}_{-1.958}$
W^-H	LO	$1.155^{+5.403}_{-5.039}$	$1.256^{+5.573}_{-5.135}$	$2.500^{+8.080}_{-7.440}$	$8.486^{+16.297}_{-16.191}$
	NLO	$1.373^{+1.602}_{-1.529}$	$1.502^{+1.531}_{-1.531}$	$3.175^{+1.417}_{-1.575}$	$11.986^{+2.928}_{-2.762}$
	NNLO	$1.419^{+1.409}_{-1.762}$	$1.550^{+1.613}_{-1.613}$	$3.318^{+1.206}_{-1.627}$	$12.837^{+1.651}_{-2.002}$
ZH	LO	$0.562^{+5.931}_{-5.931}$	$0.606^{+6.191}_{-6.191}$	$1.134^{+9.162}_{-9.162}$	$3.723^{+17.062}_{-17.062}$
	NLO	$0.680^{+2.937}_{-2.959}$	$0.737^{+3.012}_{-3.009}$	$1.461^{+4.324}_{-4.331}$	$5.246^{+7.332}_{-7.319}$
	NNLO	$0.775^{+3.454}_{-3.390}$	$0.846^{+3.637}_{-3.476}$	$1.810^{+4.089}_{-4.213}$	$7.532^{+9.144}_{-9.390}$

Table 5 LO, NLO and NNLO QCD predictions for the channels of W^+H, W^-H and ZH at $\sqrt{s} = 13$, 14, 27 and 100 TeV. For all channels W^+ decays to $e^+\nu$, W^- decays to $e^-\bar{\nu}$, Z decays to e^-e^+, H decays to $b\bar{b}$ and all units are in fb. The uncertainties were calculated taking the quadratic sum of the PDF, scale, and α_S, and provided as the percentage (±%) of the QCD results

		13 TeV	14 TeV	27 TeV	100 TeV
W^+H	LO	$25.588^{+4.420}_{-3.971}$	$27.562^{+4.710}_{-4.232}$	$49.974^{+7.875}_{-7.216}$	$141.686^{+15.940}_{-15.817}$
	NLO	$30.580^{+1.655}_{-1.467}$	$33.116^{+1.590}_{-1.420}$	$63.197^{+1.418}_{-1.507}$	$198.491^{+3.061}_{-2.817}$
	NNLO	$32.888^{+1.729}_{-1.812}$	$35.703^{+1.792}_{-1.685}$	$69.770^{+1.944}_{-1.564}$	$228.589^{+1.041}_{-2.739}$
W^-H	LO	$15.064^{+4.945}_{-4.544}$	$16.487^{+5.168}_{-4.704}$	$34.401^{+7.981}_{-7.301}$	$122.153^{+16.193}_{-16.042}$
	NLO	$17.781^{+1.524}_{-1.563}$	$19.563^{+1.484}_{-1.529}$	$43.055^{+1.312}_{-1.595}$	$170.010^{+3.042}_{-2.857}$
	NNLO	$18.700^{+1.503}_{-1.716}$	$20.630^{+1.435}_{-1.684}$	$46.351^{+1.599}_{-1.601}$	$191.738^{+1.657}_{-2.513}$
ZH	LO	$7.297^{+5.885}_{-5.885}$	$7.888^{+6.121}_{-6.121}$	$15.070^{+8.993}_{-8.993}$	$49.583^{+16.942}_{-16.942}$
	NLO	$8.755^{+2.853}_{-2.848}$	$9.519^{+3.005}_{-3.005}$	$19.222^{+4.276}_{-4.289}$	$69.555^{+7.429}_{-7.472}$
	NNLO	$10.132^{+3.616}_{-3.551}$	$11.103^{+3.578}_{-3.549}$	$24.381^{+4.729}_{-4.827}$	$104.282^{+10.654}_{-10.834}$

Table 6 LO, NLO and NNLO QCD predictions for the channels of W^+H, W^-H and ZH at $\sqrt{s} = 13$, 14, 27 and 100 TeV. For all channels W^+ decays to $e^+\nu$, W^- decays to $e^-\bar{\nu}$, Z decays to e^-e^+, H decays to γ pair and all units are in fb. The uncertainties were calculated using the quadratic sum of the PDF, scale and α_S, and provided as the QCD results percentage (±%)

		13 TeV	14 TeV	27 TeV	100 TeV
W^+H	LO	$0.064^{+4.490}_{-4.047}$	$0.068^{+4.659}_{-4.161}$	$0.117^{+7.864}_{-7.196}$	$0.336^{+15.989}_{-15.816}$
	NLO	$0.075^{+1.717}_{-1.627}$	$0.081^{+1.656}_{-1.525}$	$0.147^{+1.404}_{-1.490}$	$0.466^{+2.908}_{-2.701}$
	NNLO	$0.078^{+1.666}_{-1.402}$	$0.083^{+1.695}_{-1.340}$	$0.152^{+1.459}_{-1.167}$	$0.491^{+1.536}_{-1.879}$
W^-H	LO	$0.042^{+5.777}_{-5.421}$	$0.046^{+5.499}_{-5.235}$	$0.091^{+8.283}_{-7.614}$	$0.309^{+16.331}_{-16.217}$
	NLO	$0.049^{+2.250}_{-2.228}$	$0.054^{+2.069}_{-2.146}$	$0.113^{+1.462}_{-1.633}$	$0.427^{+3.058}_{-2.794}$
	NNLO	$0.050^{+2.182}_{-2.138}$	$0.055^{+1.878}_{-2.048}$	$0.117^{+1.321}_{-1.741}$	$0.450^{+1.419}_{-2.185}$
ZH	LO	$0.020^{+6.020}_{-6.020}$	$0.022^{+5.986}_{-5.986}$	$0.041^{+9.408}_{-9.408}$	$0.135^{+17.064}_{-17.064}$
	NLO	$0.024^{+4.850}_{-4.855}$	$0.026^{+4.658}_{-4.681}$	$0.052^{+4.450}_{-4.457}$	$0.186^{+7.122}_{-7.148}$
	NNLO	$0.027^{+4.731}_{-4.669}$	$0.030^{+4.584}_{-4.549}$	$0.064^{+4.132}_{-4.196}$	$0.265^{+9.084}_{-9.323}$

decay leptonically and the Higgs boson decays $\tau^-\tau^+$, $b\bar{b}$ and γ pair, respectively in the tables. In addition to QCD predictions, PDF, scale, and α_S uncertainties for all the channels were computed as defined in Sect. 2. The tables also include the asymmetric total uncertainty results that were calculated taking the quadratic sum of PDF, scale, and α_S uncertainties. For the detailed results of the numerical PDF, scale, and α_S, please see Appendix A (Fig. 5).

Figure 6 shows the scale uncertainty results for different scale variations. We conducted a comprehensive study for the scale uncertainty across all energies considered in this study, but only the results at $\sqrt{s}$ = 100 TeV are shared here as an example. Table 7 provides the numerical results for all channels. Normalization and factorization scales were varied independently, and the maximum absolute deviation from the default value (μ_R, μ_F) = (1,1) was assigned as the scale uncertainty. As observed for the WH channels, the scale uncertainty is highest at LO, followed by NLO and NNLO, respectively. However, this is not the case for all ZH channels. NNLO scale uncertainty is highest at the values of $(\mu_R, \mu_F) = (2, 1), (2, 1/2), (1/2, 1), (1/2, 2)$ at all ZH channels. High-order QCD predictions (NLO and NNLO) are important while calculating the cross-section of a process because they provide the results that are obtained with the addition of extra diagrams into the process. This leads to obtaining more reliable and correct results compared to the LO predictions. In addition, high-order QCDs must have low uncertainties compared to the LO uncertainties. While the numerical values of NLO and NNLO QCD predictions are higher than those of LO QCD predictions, the scale uncertainties at NLO and NNLO QCD are lower than those at LO QCD since the percentage values are taken into account. The scale and total uncertainties of the WH and ZH channels were calculated and the obtained results were plotted as a function of energy as shown in Fig. 7. In this figure, WH and ZH production channels have three different decays; W and Z have leptons in their final states and H has b quarks, tau, and gamma pairs in its final state. As shown in the figure both total and scale uncertainties decrease as the QCD level increases. In addition, total and scale uncertainties at LO increase significantly with the increasing energy, but uncertainties at NNLO show a tiny increase with the increasing energy.

NNLO QCD results given in this study do not include final state QCD radiations (FSR) because the latest version of the MCFM does not support the calculation of FSR at NNLO.

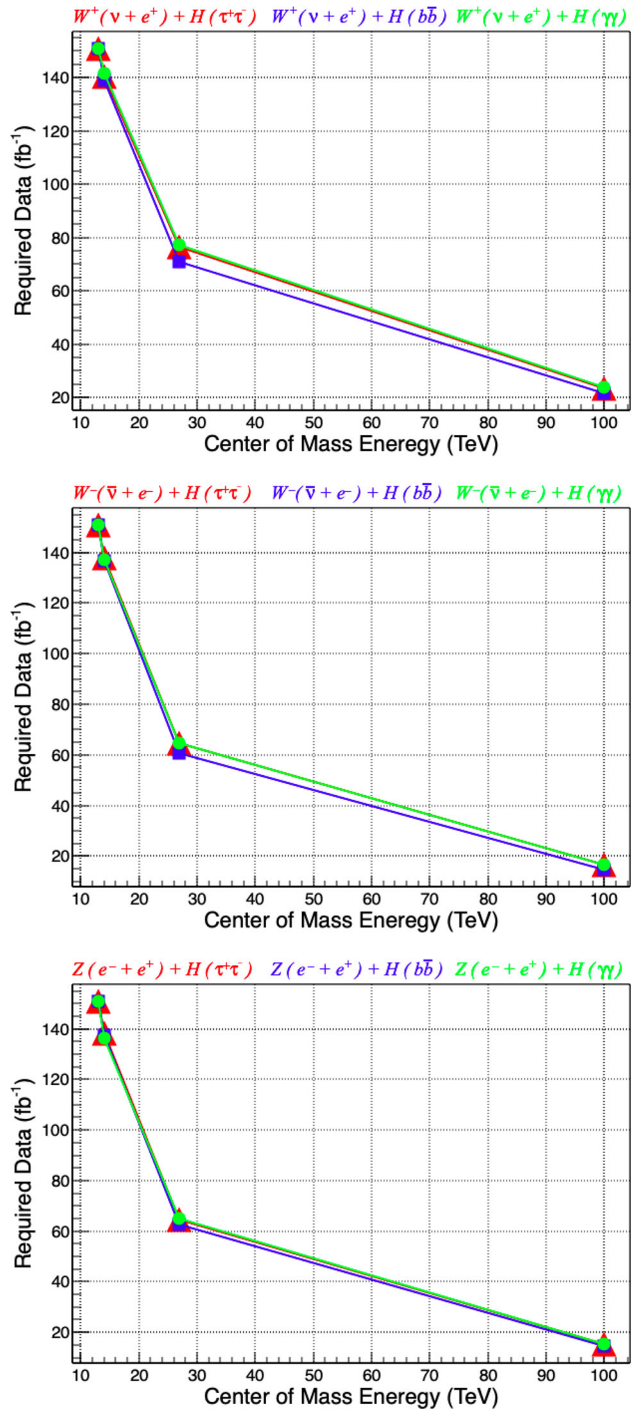

Fig. 5 The comparison of required data for the channels at $\sqrt{s}$= 14, 27, and 100 TeV to reach the same statistics with the data at $\sqrt{s}$= 13 TeV

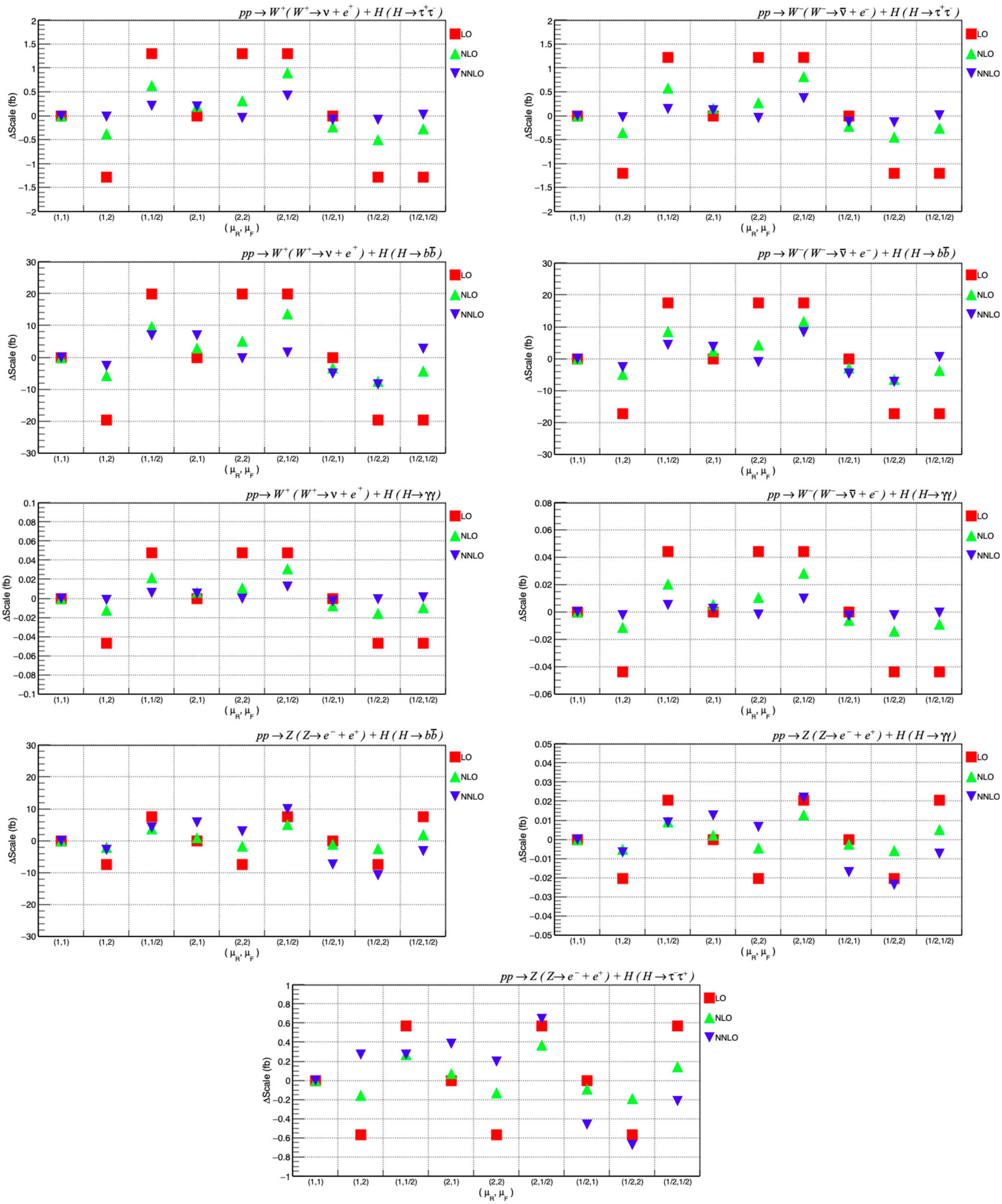

Fig. 6 Variation of μ_R and μ_F scales independently at LO, NLO and NNLO QCD. The presented data is obtained for all channels at $\sqrt{s}$ = 100 TeV

Table 7 Numerical results of highest scale uncertainty of LO, NLO and NNLO QCD at $\sqrt{s}$=13, 14, 27 and 100 TeV. All results are in the unit of fb

		13 TeV	14 TeV	27 TeV	100 TeV
$W^+ \to e^+\nu$, $W^- \to e^-\bar{\nu}$, $Z \to e^-e^+$, $H \to \tau^-\tau^+$					
W^+H	LO	0.056	0.066	0.227	1.296
	NLO	0.051	0.058	0.160	0.904
	NNLO	0.015	0.022	0.062	0.416
W^-H	LO	0.037	0.046	0.183	1.218
	NLO	0.033	0.040	0.124	0.823
	NNLO	0.013	0.008	0.045	0.368
ZH	LO	0.019	0.024	0.089	0.568
	NLO	0.018	0.020	0.060	0.370
	NNLO	0.023	0.027	0.071	0.680
$W^+ \to e^+\nu$, $W^- \to e^-\bar{\nu}$, $Z \to e^-e^+$, $H \to b\bar{b}$					
W^+H	LO	0.798	0.970	3.552	19.910
	NLO	0.746	0.859	2.496	13.748
	NNLO	0.576	0.645	1.928	8.599
W^-H	LO	0.471	0.586	2.482	17.444
	NLO	0.445	0.511	1.717	11.763
	NNLO	0.241	0.271	0.973	8.229
ZH	LO	0.242	0.296	1.149	7.491
	NLO	0.219	0.256	0.783	5.006
	NNLO	0.328	0.360	1.110	10.945
$W^+ \to e^+\nu$, $W^- \to e^-\bar{\nu}$, $Z \to e^-e^+$, $H \to \gamma\gamma$					
W^+H	LO	0.002	0.002	0.008	0.048
	NLO	0.002	0.002	0.005	0.031
	NNLO	0.000	0.002	0.001	0.012
W^-H	LO	0.001	0.002	0.007	0.045
	NLO	0.001	0.002	0.004	0.028
	NNLO	0.000	0.000	0.001	0.010
ZH	LO	0.001	0.001	0.003	0.021
	NLO	0.001	0.001	0.002	0.013
	NNLO	0.001	0.001	0.002	0.024

Due to this, we could not provide a comprehensive study for the FSR at NNLO in case of Higgs decaying into bottom quarks. However, we could calculate the FSR at NLO QCD that was obtained by using NNLO QCD PDFs. The FSR is applied within the framework of MCFM itself with the incorporation of some techniques such as zero-jettiness slicing and q_T-slicing. The Zero-jettiness slicing technique improves the management of collinear and soft-photon emission by dividing the phase space into hard and soft emissions according to a measure of jet separation (the "jettiness"). In our calculation, the Higgs boson decays into b quarks. Therefore, the q_T-slicing technique which controls soft and collinear photon emissions by slicing the transverse momentum q_T of the emitted photon is very useful since the process of Higgs decaying to b quarks involves final-state radiation from heavy quarks (b quarks). The q_T-slicing technique guarantees that photon radiation effects are accurately included in QCD calculations. Table 9 shows NLO QCD predictions including FSR corrections that are obtained by using NNLO PDF. As shown in the table, including final state QCD radiations in the NLO QCD provides slight corrections and causes insignificant reduction in the NLO QCD. A more comprehensive study for NNLO QCD with FSR is planned to be carried out in our future study which will consist of the machine learning algorithms as well.

In hadron colliders, as the collision energy increases, it is possible to obtain the same statistics as at low energies with fewer data at high energies compared to lower energy collisions. Because of this, the amount of data that would provide the same statistics at higher energies as the amount of data obtained at low energies was calculated using the relationship between cross-section and integrated luminosity

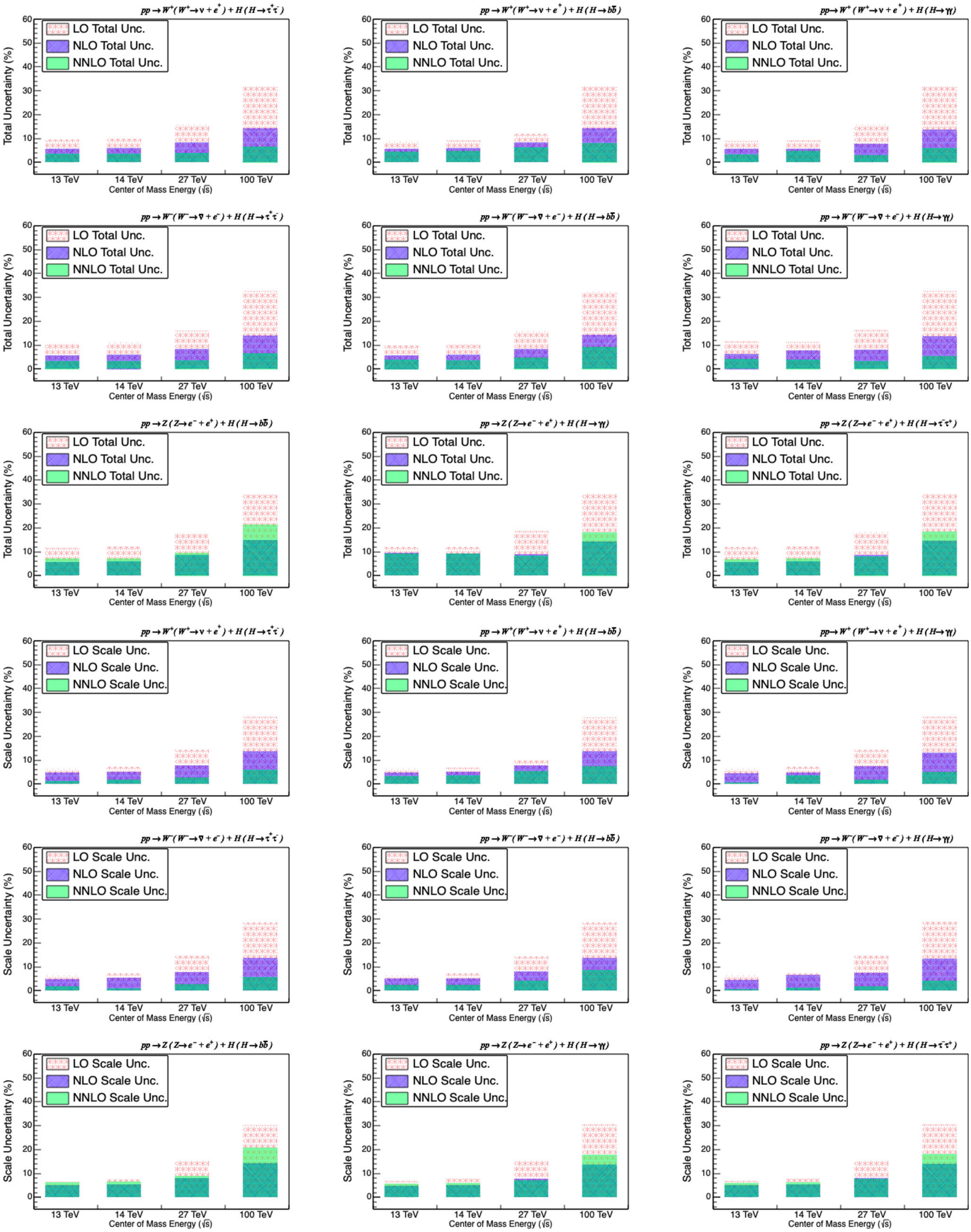

Fig. 7 Total and scale uncertainties of the WH and ZH channels as a function of center-of-mass energy and QCD orders. Both total and scale uncertainties shown in the figure are provided as the percentage (%) of the QCD orders

Table 8 The numerical values of the charge asymmetry results for different QCD orders at $\sqrt{s}$ = 13, 14, 27 and 100 TeV

Channel	Center-of-Mass Energy	LO	NLO	NNLO
$\tau^-\tau^+$	13	$0.199^{+0.057}_{-0.059}$	$0.208^{+0.021}_{-0.019}$	$0.209^{+0.020}_{-0.019}$
	14	$0.190^{+0.059}_{-0.060}$	$0.198^{+0.020}_{-0.019}$	$0.202^{+0.019}_{-0.019}$
	27	$0.121^{+0.085}_{-0.086}$	$0.126^{+0.016}_{-0.017}$	$0.127^{+0.015}_{-0.017}$
	100	$0.040^{+0.167}_{-0.167}$	$0.043^{+0.029}_{-0.030}$	$0.043^{+0.015}_{-0.021}$
$b\bar{b}$	13	$0.259^{+0.058}_{-0.053}$	$0.265^{+0.020}_{-0.019}$	$0.275^{+0.021}_{-0.023}$
	14	$0.251^{+0.061}_{-0.055}$	$0.257^{+0.019}_{-0.018}$	$0.268^{+0.021}_{-0.021}$
	27	$0.185^{+0.094}_{-0.086}$	$0.190^{+0.016}_{-0.018}$	$0.202^{+0.022}_{-0.019}$
	100	$0.040^{+0.172}_{-0.171}$	$0.077^{+0.033}_{-0.031}$	$0.088^{+0.014}_{-0.029}$
$\gamma\gamma$	13	$0.206^{+0.060}_{-0.055}$	$0.214^{+0.023}_{-0.023}$	$0.218^{+0.023}_{-0.021}$
	14	$0.196^{+0.061}_{-0.055}$	$0.204^{+0.022}_{-0.021}$	$0.207^{+0.021}_{-0.020}$
	27	$0.125^{+0.090}_{-0.083}$	$0.130^{+0.016}_{-0.018}$	$0.131^{+0.016}_{-0.016}$
	100	$0.041^{+0.168}_{-0.167}$	$0.044^{+0.031}_{-0.029}$	$0.043^{+0.015}_{-0.021}$

Table 9 NLO QCD predictions including FSR corrections that are obtained by using NNLO PDF for the Higgs boson decay into bottom quarks. The uncertainties were obtained through the calculation of the quadratic sum of PDF, scale and α_S, and given as the percentage (%) of the QCD results

		13 TeV	14 TeV	27 TeV	100 TeV
W^+H	NLO QCD with FSR corrections	$31.094^{+1.789}_{-1.478}$	$33.690^{+1.681}_{-1.435}$	$64.506^{+1.389}_{-1.500}$	$203.085^{+2.803}_{-2.836}$
	FSR correction (%)	−0.0003	−0.0005	−0.0001	−0.0003
W^-H	NLO QCD with FSR corrections	$17.982^{+1.708}_{-1.536}$	$19.808^{+1.620}_{-1.500}$	$43.903^{+1.353}_{-1.555}$	$174.399^{+2.863}_{-2.835}$
	FSR correction (%)	−0.001	−0.001	−0.001	−0.0004
ZH	NLO QCD with FSR corrections	$8.872^{+6.316}_{-5.910}$	$9.656^{+6.469}_{-5.879}$	$19.625^{+7.606}_{-5.245}$	$71.271^{+9.222}_{-3.470}$
	FSR correction (%)	−0.001	−0.001	−0.0004	−0.008

($N = \sigma x L$). Since the highest order prediction calculated for all production channels in this study is the NNLO QCD, it was used for the cross-section value in this calculation. Therefore, NNLO QCD predictions calculated at $\sqrt{s} = 13$ TeV were taken into account to calculate the required data at $\sqrt{s} = 14$, 27 and 100 TeV to obtain the same statistics with the data at $\sqrt{s} = 13$ TeV.

During Run 2 (2015–2018) the total amount of data recorded by the CMS detector at $\sqrt{s} = 13$ TeV is 150.78 fb^{-1} [54]. Taking this into account the required data at $\sqrt{s} = 14$, 27 and 100 TeV that provide the same statistics as the data at $\sqrt{s} = 13$ TeV were calculated and the numerical results are given in Table 10. A comparison of the amount of data that needs to be obtained at high energies is shown in Fig. 5. As the energy increases, less data is needed at high energies to obtain the same number of events obtained with the data at low energies. Specifically, the same statistics can be obtained at $\sqrt{s}$ = 14, 27, and 100 TeV with approximately 1.1, 2.0 and 6.5 times less data than the amount of data at $\sqrt{s}$ = 13 TeV, respectively. This shows that higher energies provide advantages not only in the study of new physics research and the observation of new particles but also in the measurements of known particles.

Table 10 A comparison of the amount of data (fb^{-1}) that needs to be obtained at high energies to reach the same statistics with the data obtained at $\sqrt{s} = 13$ TeV

	14 TeV	27 TeV	100 TeV
$W^+(e^+\nu) + H(\tau^-\tau^+)$	140.245	76.447	23.408
$W^+(e^+\nu) + H(b\bar{b})$	138.892	71.074	21.693
$W^+(e^+\nu) + H(\gamma\gamma)$	141.697	77.374	23.953
$W^-(e^-\bar{\nu}) + H(\tau^-\tau^+)$	138.037	64.484	16.667
$W^-(e^-\bar{\nu}) + H(b\bar{b})$	136.674	60.831	14.705
$W^-(e^-\bar{\nu}) + H(\gamma\gamma)$	137.073	64.436	16.753
$Z(e^-e^+) + H(\tau^-\tau^+)$	138.114	64.493	15.509
$Z(e^-e^+) + H(b\bar{b})$	137.472	62.661	14.658
$Z(e^-e^+) + H(\gamma\gamma)$	136.188	64.951	15.521

On the production of a Higgs boson in association with a W boson, there are possible channels with respect to the subsequent decay modes of both the W boson and the Higgs

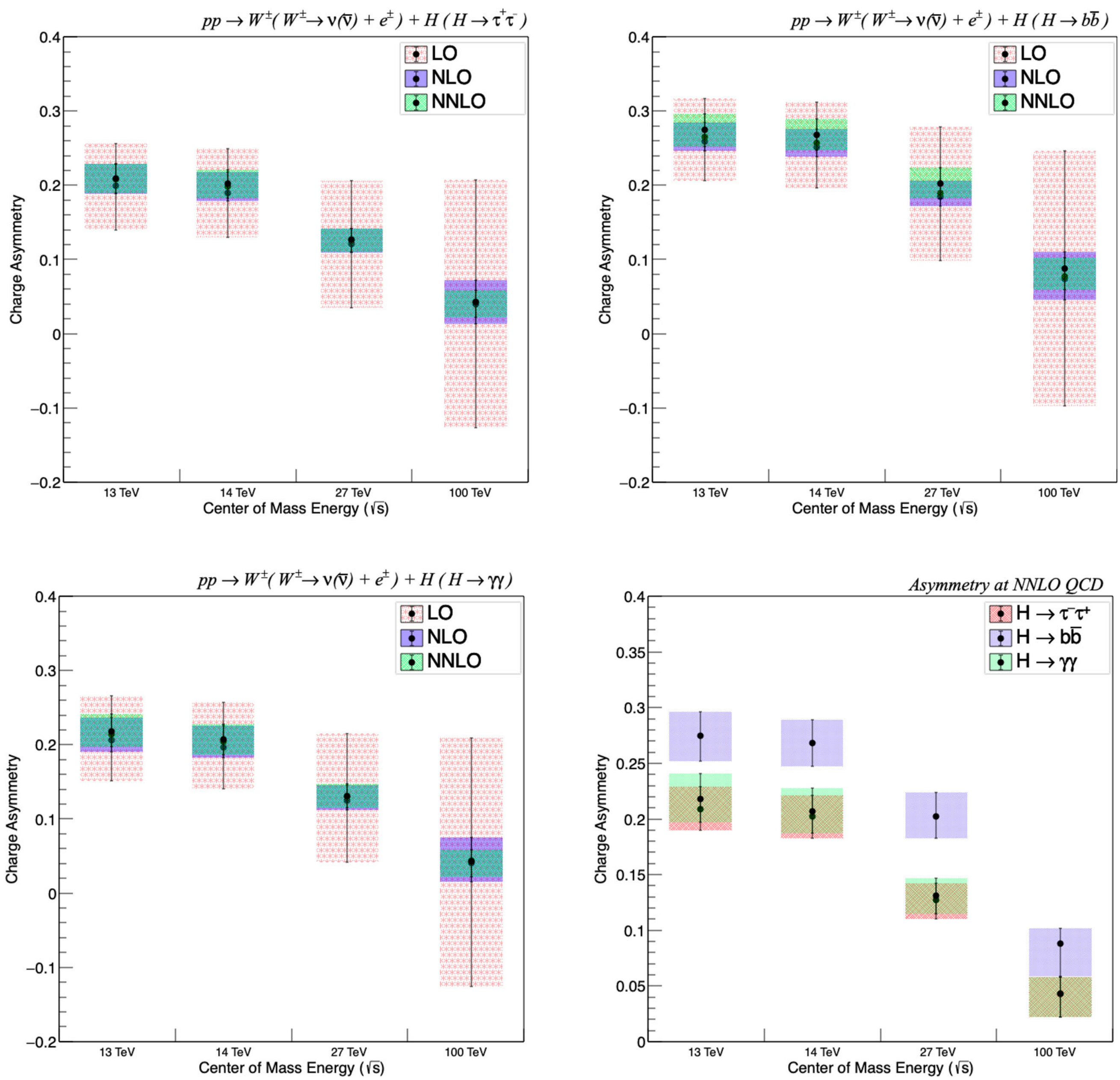

Fig. 8 The comparison of charge asymmetry results at different QCD orders and the comparison of charge asymmetry results obtained for different channel

boson. In the presented study, the considered subsequent particle for W boson is electron while $\tau^-\tau^+$, $b\bar{b}$ or $\gamma\gamma$ channels are chosen as sub decay particles for Higgs boson. Based on the numbers tabulated in Tables 3, 4 and 5, W boson charge asymmetry could be easily computed as a function of center-of-mass energy using the following equation:

$$A_W = \frac{\sigma_{W^+} - \sigma_{W^-}}{\sigma_{W^+} + \sigma_{W^-}} \tag{8}$$

The charge asymmetry of LO, NLO, and NNLO QCD were calculated for all decay channels considered in this paper. Figure 8 shows a comparison of the charge asymmetry at different QCD orders. For all the channels, the asymmetry of LO, NLO, and NNLO QCD decreases with the increasing center-of-mass energy, but the total uncertainty arising from PDF, scale, and α_S is extremely huge at LO charge asymmetry, especially at $\sqrt{s}$ = 100 TeV. Contrary to LO asymmetry, NLO and NNLO asymmetries have small uncertainties. NNLO QCD has the highest asymmetry and the smallest uncertainty compared to the LO and NLO asymmetries. Despite the increase in the asymmetry result, the decrease in uncertainty shows that NNLO QCD gives more accurate and reliable results in high-energy experiments to compare with experimental data. The numerical values of the charge asymmetry result at different QCD orders for all channels are given in Table 8. Figure 8 (bottom right) illustrates a comparison of charge asymmetry results obtained at NNLO QCD for different channels. The lowest charge asymmetry between W^+ and W^- channels is obtained with $WH(\tau^-\tau^+)$ decays while a greater asymmetry compares to the other two channels observed for $WH(b\bar{b})$ events. This asymmetry difference arises due to the structure of the colliding protons. The lowest asymmetry for the $\tau\tau$ channel indicates that the parton-level asymmetry from W^+ and W^- production has less effect on the τ-jet observables. This disparity in the charge asymmetry emphasizes the importance of jet definition and reconstruction methods for understanding charge asymmetries. The asymmetry significantly decreases with the increase of center-of-mass energy. The reduction of charge asymmetry with the increasing center-of-mass energy is due to the increased contribution of sea quarks and the smaller difference between the u- and d-quark distributions at small momentum fraction of partons. The asymmetries for $WH(\tau^-\tau^+)$, $WH(\gamma\gamma)$ and $WH(b\bar{b})$ events at $\sqrt{s}$ = 13 TeV are about 4.9, 5.0 and 3.1 times greater than the ones at $\sqrt{s}$ = 100 TeV. Further precise measurements of the charge asymmetry could provide insights into the structure of protons, the behavior of quarks and gluons inside protons, and the properties of the Higgs boson and Higgs couplings to other particles.

3.1 The comparison with the available reference results

Table 11 provides a comparison of our results with the available reference results provided in the Ref. [55]. As shown in the table, our $\sqrt{s}$ = 13 TeV NNLO results are higher than the reference predictions at the same center of mass energy provided in Ref. [55]. The reason for this inconsistency is the slight difference in the selection cuts of the reference calculations and our predictions. Moreover, reference results in Ref. [55] were obtained by using CT14 PDF while we used the most modern one, NNPDF3.1. Since the PDFs are based on different parameterizations and choices of input data, resulting in variations in the parton distribution at different energy scales, the choice of the PDFs may change the QCD cross-sections. In addition to the different selection cuts, the different parameterizations and underlying experimental data used to derive the PDFs may be responsible for the discrepancy in the computed QCD cross-sections. In contrast to the CT14 set, the NNPDF3.1 set treats parton distributions differently, especially for gluons and lighter quarks. This results in differences in the parton-parton luminosity, which impacts the cross-section computation.

Table 11 The numerical values of our results (NNLO QCD) and available reference predictions [55]

	NNLO QCD (fb)	Ref. [55] (fb)	Ratio
W^+H	$32.888^{+1.729}_{-1.812}$	$24.180^{+0.360}_{-0.640}$	1.360
W^-H	$18.700^{+1.503}_{-1.716}$	$15.870^{+0.270}_{-0..460}$	1.178
ZH	$10.132^{+3.616}_{-3.551}$	$6.891^{+0.101}_{-0.162}$	1.470

4 Conclusion

In this study, we present an analysis of QCD predictions for the simultaneous production of vector and Higgs bosons at $\sqrt{s}$ = 13, 14, 27 and 100 TeV, which are relevant for the LHC and future high-energy colliders. Through sophisticated simulation methods and the integration of the MCFM program within high-performance computing frameworks, we have advanced our understanding of the branching states of vector and Higgs bosons under high-order QCD predictions. Our findings contribute not only to the theoretical predictions within the SM but also provide a critical foundation for future experimental explorations at the LHC and beyond. Specifically, in the context of Higgs studies, the energy increase allows for more precise measurements of the Higgs properties and interactions, enabling the exploration of rare decay channels and potential deviations from the SM predictions. Such studies could uncover new physics beyond the SM, providing deeper insights into the mechanism of electroweak symmetry breaking and the origins of mass.

Acknowledgements This study was funded by the Scientific and Technological Research Council of Turkey (TUBITAK) 1002-A Grant No 122F270. The numerical calculations reported in this paper were fully/partially performed at TUBITAK ULAKBIM, High Performance and Grid Computing Center (TRUBA resources). Dr. Emrah Tiras is thankful for the support of the Turkish Academy of Sciences (TUBA) under the Outstanding Young Scientists Awards Program (GEBIP) grant.

Data Availability Statement Data will be made available on reasonable request. [Authors' comment: The datasets generated during and/or analysed during the current study are available from the corresponding author on reasonable request.]

Code Availability Statement This manuscript has no associated code/software. [Authors' comment: Code/Software sharing not applicable to this article as no code/software was generated or analysed during the current study.]

Funded by SCOAP[3].

Appendix A: The numerical results for PDF, scale and α_S uncertainties at $\sqrt{s}$ = 13, 14, 27 and 100 TeV

See Tables 12, 13 and 14.

Table 12 PDF uncertainties for the production channels. All results are in the units of fb and given as the percentage (±%) of the QCD results

		13 TeV	14 TeV	27 TeV	100 TeV
$W^+ \to e^+\nu$, $W^- \to e^-\bar{\nu}$, $Z \to e^-e^+$, $H \to \tau^-\tau^+$					
W^+H	LO	± 3.524	± 3.465	± 2.793	± 2.416
	NLO	± 1.289	± 1.202	± 0.709	± 0.689
	NNLO	± 1.244	± 1.157	± 0.678	± 0.079
W^-H	LO	± 4.329	± 4.220	± 2.840	± 2.722
	NLO	± 1.165	± 1.132	± 0.693	± 0.651
	NNLO	± 1.268	± 1.290	± 0.680	± 0.608
ZH	LO	± 4.801	± 4.789	± 4.321	± 3.089
	NLO	± 1.176	± 1.085	± 0.684	± 1.010
	NNLO	± 1.290	± 1.182	± 0.663	± 1.155
$W^+ \to e^+\nu$, $W^- \to e^-\bar{\nu}$, $Z \to e^-e^+$, $H \to b\bar{b}$					
W^+H	LO	± 3.126	± 3.109	± 2.573	± 1.927
	NLO	± 1.171	± 1.117	± 0.699	± 0.632
	NNLO	± 1.192	± 1.120	± 0.738	± 0.589
W^-H	LO	± 3.817	± 3.748	± 3.744	± 2.204
	NLO	± 1.130	± 1.079	± 0.699	± 0.593
	NNLO	± 1.214	± 1.144	± 0.701	± 0.754
ZH	LO	± 4.838	± 4.830	± 4.353	± 2.959
	NLO	± 1.131	± 1.072	± 0.645	± 0.927
	NNLO	± 1.194	± 1.108	± 0.664	± 1.432
$W^+ \to e^+\nu$, $W^- \to e^-\bar{\nu}$, $Z \to e^-e^+$, $H \to \gamma\gamma$					
W^+H	LO	± 3.125	± 2.941	± 2.564	± 2.381
	NLO	± 1.333	± 1.235	± 0.680	± 0.644
	NNLO	± 1.282	± 1.205	± 0.658	± 0.611
W^-H	LO	± 4.762	± 4.348	± 3.297	± 2.589
	NLO	± 2.041	± 1.852	± 0.885	± 0.703
	NNLO	± 2.000	± 1.818	± 0.855	± 0.667
ZH	LO	± 4.900	± 4.550	± 4.859	± 2.967
	NLO	± 4.129	± 3.810	± 1.925	± 1.077
	NNLO	± 3.663	± 3.350	± 1.568	± 0.755

Table 13 Scale uncertainties for the production channels. All results are in the units of fb and given as the percentage (±%) of the QCD results

		13 TeV	14 TeV	27 TeV	100 TeV
$W^+ \to e^+\nu$, $W^- \to e^-\bar{\nu}$, $Z \to e^-e^+$, $H \to \tau^-\tau^+$					
W^+H	LO	± 3.224	± 3.589	± 7.136	± 14.101
	NLO	± 2.437	± 2.599	± 3.906	± 6.921
	NNLO	± 0.688	± 0.941	± 1.443	± 2.974
W^-H	LO	± 3.209	± 3.627	± 7.313	± 14.354
	NLO	± 2.416	± 2.693	± 3.917	± 6.871
	NNLO	± 0.894	± 0.538	± 1.367	± 2.864
ZH	LO	± 3.461	± 3.921	± 7.821	± 15.263
	NLO	± 2.580	± 2.690	± 4.122	± 7.051
	NNLO	± 3.028	± 3.204	± 3.898	± 9.023
$W^+ \to e^+\nu$, $W^- \to e^-\bar{\nu}$, $Z \to e^-e^+$, $H \to b\bar{b}$					
W^+H	LO	± 3.119	± 3.520	± 4.995	± 14.052
	NLO	± 2.441	± 2.593	± 3.950	± 6.926
	NNLO	± 1.752	± 1.808	± 2.763	± 3.726
W^-H	LO	± 3.130	± 3.557	± 7.216	± 14.280
	NLO	± 2.503	± 2.611	± 3.987	± 6.919
	NNLO	± 1.291	± 1.313	± 2.099	± 4.292
ZH	LO	± 3.319	± 3.753	± 7.624	± 15.107
	NLO	± 2.503	± 2.688	± 4.073	± 7.197
	NNLO	± 3.240	± 3.246	± 4.552	± 10.496
$W^+ \to e^+\nu$, $W^- \to e^-\bar{\nu}$, $Z \to e^-e^+$, $H \to \gamma\gamma$					
W^+H	LO	± 3.206	± 3.611	± 7.151	± 14.196
	NLO	± 2.314	± 2.453	± 3.728	± 6.623
	NNLO	± 0.408	± 1.841	± 0.907	± 2.534
W^-H	LO	± 3.226	± 3.661	± 7.334	± 14.398
	NLO	± 2.334	± 3.310	± 3.806	± 6.651
	NNLO	± 0.368	± 0.659	± 0.996	± 2.161
ZH	LO	± 3.472	± 3.886	± 7.797	± 15.283
	NLO	± 2.438	± 2.579	± 3.851	± 6.847
	NNLO	± 2.823	± 3.009	± 3.684	± 9.016

Table 14 α_S uncertainties for the production channels. All results are in the units of fb and given as the percentage (±%) of the QCD results

		13 TeV	14 TeV	27 TeV	100 TeV
$W^+ \to e^+\nu$, $W^- \to e^-\bar{\nu}$, $Z \to e^-e^+$, $H \to \tau^-\tau^+$					
W^+H	LO	+ 0.050 − 0.050	+ 0.258 − 0.258	+ 2.012 − 2.012	+ 6.982 − 6.982
	NLO	+ 0.866 − 0.824	+ 0.911 − 0.935	+ 1.207 − 1.208	+ 1.604 − 1.612
	NNLO	+ 1.252 − 0.684	+ 1.012 − 0.837	+ 1.113 − 1.192	+ 1.230 − 1.950
W^-H	LO	+ 0.432 − 0.432	+ 0.217 − 0.217	+ 1.996 − 1.996	+ 7.229 − 7.229
	NLO	+ 0.758 − 0.906	+ 0.761 − 1.049	+ 1.221 − 1.222	+ 1.661 − 1.523
	NNLO	+ 0.501 − 1.156	+ 0.816 − 0.941	+ 0.892 − 1.435	+ 1.490 − 1.904
ZH	LO	+ 0.389 − 0.389	+ 0.167 − 0.167	+ 2.026 − 2.026	+ 6.973 − 6.973
	NLO	+ 0.765 − 0.848	+ 0.809 − 0.801	+ 1.109 − 1.137	+ 1.735 − 1.678
	NNLO	+ 1.047 − 0.809	+ 1.250 − 0.649	+ 1.042 − 1.454	+ 0.931 − 2.331
$W^+ \to e^+\nu$, $W^- \to e^-\bar{\nu}$, $Z \to e^-e^+$, $H \to b\bar{b}$					
W^+H	LO	+ 0.188 − 0.188	+ 0.367 − 0.367	+ 2.206 − 2.206	+ 7.273 − 7.273
	NLO	+ 0.850 − 0.844	+ 0.883 − 0.862	+ 1.210 − 1.201	+ 1.588 − 1.729
	NNLO	+ 0.913 − 0.865	+ 1.047 − 0.925	+ 1.423 − 1.198	+ 0.846 − 2.381
W^-H	LO	+ 0.291 − 0.291	+ 0.081 − 0.081	+ 2.025 − 2.025	+ 7.309 − 7.309
	NLO	+ 0.669 − 1.051	+ 0.745 − 1.073	+ 1.098 − 1.291	+ 1.617 − 1.687
	NNLO	+ 0.564 − 1.094	+ 0.599 − 1.087	+ 1.082 − 1.391	+ 1.359 − 2.378
ZH	LO	+ 0.458 − 0.458	+ 0.226 − 0.226	+ 1.949 − 1.949	+ 7.075 − 7.075
	NLO	+ 0.771 − 0.755	+ 0.810 − 0.809	+ 1.132 − 1.178	+ 1.591 − 1.783
	NNLO	+ 1.072 − 0.825	+ 1.020 − 0.912	+ 1.097 − 1.463	+ 1.141 − 2.273
$W^+ \to e^+\nu$, $W^- \to e^-\bar{\nu}$, $Z \to e^-e^+$, $H \to \gamma\gamma$					
W^+H	LO	+ 0.066 − 0.066	+ 0.236 − 0.236	+ 2.030 − 2.030	+ 6.976 − 6.976
	NLO	+ 0.835 − 0.912	+ 0.852 − 0.884	+ 1.217 − 1.163	+ 1.598 − 1.559
	NNLO	+ 0.972 − 0.546	+ 1.081 − 0.559	+ 1.199 − 0.964	+ 1.407 − 1.769
W^-H	LO	+ 0.458 − 0.458	+ 0.226 − 0.226	+ 1.972 − 1.972	+ 7.229 − 7.229
	NLO	+ 0.703 − 0.999	+ 0.752 − 1.033	+ 1.096 − 1.179	+ 1.576 − 1.667
	NNLO	+ 0.768 − 0.725	+ 0.469 − 0.935	+ 0.965 − 1.510	+ 1.195 − 2.079
ZH	LO	+ 0.423 − 0.423	+ 0.144 − 0.144	+ 2.028 − 2.028	+ 6.986 − 6.986
	NLO	+ 0.726 − 0.755	+ 0.727 − 0.862	+ 1.125 − 1.155	+ 1.635 − 1.746
	NNLO	+ 0.995 − 0.640	+ 0.857 − 0.646	+ 1.022 − 1.255	+ 0.805 − 2.248

References

1. T. Aaltonen et al., Combined CDF and D0 upper limits on Standard Model Higgs boson production with up to 8.2 fb^{-1} of data. in 46th Rencontres de Moriond on Electroweak Interactions and Unified Theories (2011)
2. G. Aad et al., Observation of a new particle in the search for the Standard Model Higgs boson with the ATLAS detector at the LHC. Phys. Lett. B **716**, 1–29 (2012). https://doi.org/10.1016/j.physletb.2012.08.020. arXiv:1207.7214 [hep-ex]
3. S. Chatrchyan et al., Observation of a new Boson at a mass of 125 GeV with the CMS Experiment at the LHC. Phys. Lett. B **716**, 30–61 (2012). https://doi.org/10.1016/j.physletb.2012.08.021. arXiv:1207.7235 [hep-ex]
4. G. Aad et al., Combined measurement of the Higgs boson mass in pp collisions at $\sqrt{s} = 7$ and 8 TeV with the ATLAS and CMS Experiments. Phys. Rev. Lett. **114**, 191803 (2015). https://doi.org/10.1103/PhysRevLett.114.191803. arXiv:1503.07589 [hep-ex]
5. G. Aad et al., Measurements of the Higgs boson production and decay rates and constraints on its couplings from a combined ATLAS and CMS analysis of the LHC pp collision data at $\sqrt{s} = 7$ and 8 TeV. JHEP **08**, 045 (2016). https://doi.org/10.1007/JHEP08(2016)045. arXiv:1606.02266 [hep-ex]
6. M. Aaboud et al., Measurement of inclusive and differential cross sections in the $H \to ZZ^* \to 4\ell$ decay channel in pp collisions at $\sqrt{s} = 13$ TeV with the ATLAS detector. JHEP **10**, 132 (2017). https://doi.org/10.1007/JHEP10(2017)132. arXiv:1708.02810 [hep-ex]
7. M. Aaboud et al., Measurements of Higgs boson properties in the diphoton decay channel with 36 fb^{-1} of pp collision data at $\sqrt{s} =$ 13 TeV with the ATLAS detector. Phys. Rev. D **98**, 052005 (2018). https://doi.org/10.1103/PhysRevD.98.052005. arXiv:1802.04146 [hep-ex]
8. M. Aaboud et al., Measurement of the Higgs boson coupling properties in the $H \to ZZ^* \to 4\ell$ decay channel at $\sqrt{s} = 13$ TeV with the ATLAS detector. JHEP **03**, 095 (2018). https://doi.org/10.1007/JHEP03(2018)095. arXiv:1712.02304 [hep-ex]
9. M. Aaboud et al., Measurement of the Higgs boson mass in the $H \to ZZ^* \to 4\ell$ and $H \to \gamma\gamma$ channels with $\sqrt{s} = 13$ TeV pp collisions using the ATLAS detector. Phys. Lett. B **784**,

345–366 (2018). https://doi.org/10.1016/j.physletb.2018.07.050. arXiv:1806.00242 [hep-ex]
10. Combined measurement of the total and differential cross sections in the $H \to \gamma\gamma$ and the $H \to ZZ^* \to 4\ell$ decay channels at $\sqrt{s}$ =13 TeV with the ATLAS detector. Technical Report, CERN, Geneva (2019). https://cds.cern.ch/record/2682844
11. M. Aaboud et al., Observation of Higgs boson production in association with a top quark pair at the LHC with the ATLAS detector. Phys. Lett. B **784**, 173–191 (2018). https://doi.org/10.1016/j.physletb.2018.07.035. arXiv:1806.00425 [hep-ex]
12. M. Aaboud et al., Measurements of gluon-gluon fusion and vector-boson fusion Higgs boson production cross-sections in the $H \to WW^* \to e\nu\mu\nu$ decay channel in pp collisions at $\sqrt{s}$ = 13 TeV with the ATLAS detector. Phys. Lett. B **789**, 508–529 (2019). https://doi.org/10.1016/j.physletb.2018.11.064. arXiv:1808.09054 [hep-ex]
13. M. Aaboud et al., Cross-section measurements of the Higgs boson decaying into a pair of τ-leptons in proton-proton collisions at $\sqrt{s}$ = 13 TeV with the ATLAS detector. Phys. Rev. D **99**, 072001 (2019). https://doi.org/10.1103/PhysRevD.99.072001. arXiv:1811.08856 [hep-ex]
14. A.M. Sirunyan et al., Measurements of properties of the Higgs boson decaying into the four-lepton final state in pp collisions at $\sqrt{s}$ = 13 TeV. JHEP **11**, 047 (2017). https://doi.org/10.1007/JHEP11(2017)047. arXiv:1706.09936 [hep-ex]
15. A.M. Sirunyan et al., Measurements of Higgs boson properties in the diphoton decay channel in proton-proton collisions at $\sqrt{s}$ = 13 TeV. JHEP **11**, 185 (2018). https://doi.org/10.1007/JHEP11(2018)185. arXiv:1804.02716 [hep-ex]
16. A.M. Sirunyan et al., Observation of the Higgs boson decay to a pair of τ leptons with the CMS detector. Phys. Lett. B **779**, 283–316 (2018). https://doi.org/10.1016/j.physletb.2018.02.004. arXiv:1708.00373 [hep-ex]
17. A.M. Sirunyan et al., Observation of $t\bar{t}$H production. Phys. Rev. Lett. **120**(23), 231801 (2018). https://doi.org/10.1103/PhysRevLett.120.231801. arXiv:1804.02610 [hep-ex]
18. G. Aad et al., Measurements of the Higgs boson inclusive and differential fiducial cross-sections in the diphoton decay channel with pp collisions at $\sqrt{s}$ = 13 TeV with the ATLAS detector. JHEP **08**, 027 (2022). https://doi.org/10.1007/JHEP08(2022)027. arXiv:2202.00487 [hep-ex]
19. A.M. Sirunyan et al., Measurements of properties of the Higgs boson decaying to a W boson pair in pp collisions at $\sqrt{s}$ = 13 TeV. Phys. Lett. B **791**, 96 (2019). https://doi.org/10.1016/j.physletb.2018.12.073. arXiv:1806.05246 [hep-ex]
20. CERN: high-luminosity LHC. https://home.cern/science/accelerators/high-luminosity-lhc
21. R. Abdul Khalek et al., The physics potential of HL-LHC. https://twiki.cern.ch/twiki/pub/LHCPhysics/HLHELHCWorkshop/report.pdf
22. R. Abdul Khalek et al., The physics potential of HE-LHC. https://twiki.cern.ch/twiki/pub/LHCPhysics/HLHELHCWorkshop/HEreport.pdf
23. A. Abada, M. Abbrescia, FCC physics opportunities: future circular collider conceptual design report volume 1. Eur. Phys. J. C **79**(6), 474 (2019). https://doi.org/10.1140/epjc/s10052-019-6904-3
24. M. Aaboud et al., Evidence for the $H \to b\bar{b}$ decay with the ATLAS detector. JHEP **12**, 024 (2017). https://doi.org/10.1007/JHEP12(2017)024. arXiv:1708.03299 [hep-ex]
25. A.M. Sirunyan et al., Observation of Higgs boson decay to bottom quarks. Phys. Rev. Lett. **121**(12), 121801 (2018). https://doi.org/10.1103/PhysRevLett.121.121801. arXiv:1808.08242 [hep-ex]
26. M. Aaboud et al., Observation of $H \to b\bar{b}$ decays and VH production with the ATLAS detector. Phys. Lett. B **786**, 59–86 (2018). https://doi.org/10.1016/j.physletb.2018.09.013. arXiv:1808.08238 [hep-ex]
27. G. Ferrera, M. Grazzini, F. Tramontano, Higher-order QCD effects for associated WH production and decay at the LHC. JHEP **04**, 039 (2014). https://doi.org/10.1007/JHEP04(2014)039. arXiv:1312.1669 [hep-ph]
28. A.M. Sirunyan et al., Measurements of Higgs boson production cross sections and couplings in the diphoton decay channel at $\sqrt{s}$ = 13 TeV. JHEP **07**, 027 (2021). https://doi.org/10.1007/JHEP07(2021)027. arXiv:2103.06956 [hep-ex]
29. J. Rosenzweig, Higgs boson mass measurement using $H \to ZZ \to 4\ell$ decays at CMS. In: Meeting of the Division of Particles and Fields of the American Physical Society (2019)
30. P. Azzi et al., Report from Working Group 1: Standard Model physics at the HL-LHC and HE-LHC. CERN Yellow Rep. Monogr. **7**, 1–220 (2019). https://doi.org/10.23731/CYRM-2019-007.1. arXiv:1902.04070 [hep-ph]
31. M. Cepeda et al., Report from Working Group 2: Higgs physics at the HL-LHC and HE-LHC. CERN Yellow Rep. Monogr. **7**, 221–584 (2019). https://doi.org/10.23731/CYRM-2019-007.221. arXiv:1902.00134 [hep-ph]
32. X. Cid Vidal et al., Report from Working Group 3: beyond the Standard Model physics at the HL-LHC and HE-LHC. CERN Yellow Rep. Monogr. **7**, 585–865 (2019). https://doi.org/10.23731/CYRM-2019-007.585. arXiv:1812.07831 [hep-ph]
33. A. Cerri et al., Report from Working Group 4: opportunities in flavour physics at the HL-LHC and HE-LHC. CERN Yellow Rep. Monogr. **7**, 867–1158 (2019). https://doi.org/10.23731/CYRM-2019-007.867. arXiv:1812.07638 [hep-ph]
34. Z. Citron et al., Report from Working Group 5: future physics opportunities for high-density QCD at the LHC with heavy-ion and proton beams. CERN Yellow Rep. Monogr. **7**, 1159–1410 (2019). https://doi.org/10.23731/CYRM-2019-007.1159. arXiv:1812.06772 [hep-ph]
35. M.L. Ciccolini, S. Dittmaier, M. Kramer, Electroweak radiative corrections to associated WH and ZH production at hadron colliders. Phys. Rev. D **68**, 073003 (2003). https://doi.org/10.1103/PhysRevD.68.073003. arXiv:hep-ph/0306234
36. O. Brein, A. Djouadi, R. Harlander, NNLO QCD corrections to the Higgs-strahlung processes at hadron colliders. Phys. Lett. B **579**, 149–156 (2004). https://doi.org/10.1016/j.physletb.2003.10.112. arXiv:hep-ph/0307206
37. A. Denner, S. Dittmaier, S. Kallweit, A. Muck, Electroweak corrections to Higgs-strahlung off W/Z bosons at the Tevatron and the LHC with HAWK. JHEP **03**, 075 (2012). https://doi.org/10.1007/JHEP03(2012)075. arXiv:1112.5142 [hep-ph]
38. A. Denner, S. Dittmaier, S. Kallweit, A. Mück, HAWK 2.0: a Monte Carlo program for Higgs production in vector-boson fusion and Higgs strahlung at hadron colliders. Comput. Phys. Commun. **195**, 161–171 (2015). https://doi.org/10.1016/j.cpc.2015.04.021. arXiv:1412.5390 [hep-ph]
39. L. Altenkamp, S. Dittmaier, R.V. Harlander, H. Rzehak, T.J.E. Zirke, Gluon-induced Higgs-strahlung at next-to-leading order QCD. JHEP **02**, 078 (2013). https://doi.org/10.1007/JHEP02(2013)078. arXiv:1211.5015 [hep-ph]
40. R.V. Harlander, A. Kulesza, V. Theeuwes, T. Zirke, Soft gluon resummation for gluon-induced Higgs strahlung. JHEP **11**, 082 (2014). https://doi.org/10.1007/JHEP11(2014)082. arXiv:1410.0217 [hep-ph]
41. R.V. Harlander, J. Klappert, S. Liebler, L. Simon, vh@nnlo-v2: new physics in Higgs strahlung. JHEP **05**, 089 (2018). https://doi.org/10.1007/JHEP05(2018)089. arXiv:1802.04817 [hep-ph]
42. O. Brein, R. Harlander, M. Wiesemann, T. Zirke, Top-quark mediated effects in hadronic Higgs-strahlung. Eur. Phys. J. C **72**, 1868 (2012). https://doi.org/10.1140/epjc/s10052-012-1868-6. arXiv:1111.0761 [hep-ph]
43. G. Ferrera, M. Grazzini, F. Tramontano, Associated WH production at hadron colliders: a fully exclusive QCD calculation at

NNLO. Phys. Rev. Lett. **107**, 152003 (2011). https://doi.org/10.1103/PhysRevLett.107.152003. arXiv:1107.1164 [hep-ph]
44. G. Ferrera, M. Grazzini, F. Tramontano, Associated ZH production at hadron colliders: the fully differential NNLO QCD calculation. Phys. Lett. B **740**, 51–55 (2015). https://doi.org/10.1016/j.physletb.2014.11.040. arXiv:1407.4747 [hep-ph]
45. J. Barbara, Perturbative (QCD) calculations. https://indico.psi.ch/event/8227/contributions/21155/attachments/22431/39331/qcd-lecture.pdf
46. J.M. Campbell et al., MCFM-10.3 manual. https://mcfm.fnal.gov/manual.pdf
47. A. Buckley, J. Ferrando, S. Lloyd, K. Nordström, B. Page, M. Rüfenacht, M. Schönherr, G. Watt, LHAPDF6: parton density access in the LHC precision era. Eur. Phys. J. C **75**, 132 (2015). https://doi.org/10.1140/epjc/s10052-015-3318-8. arXiv:1412.7420 [hep-ph]
48. R.D. Ball et al., Parton distributions from high-precision collider data. Eur. Phys. J. C **77**(10), 663 (2017). https://doi.org/10.1140/epjc/s10052-017-5199-5. arXiv:1706.00428 [hep-ph]
49. T. Plehn, LHC phenomenology for physics hunters. In: Theoretical Advanced Study Institute in Elementary Particle Physics: The Dawn of the LHC Era (2010), pp. 125–180. https://doi.org/10.1142/9789812838360_0003
50. G. Aad et al., Measurements of WH and ZH production in the $H \to b\bar{b}$ decay channel in pp collisions at 13 TeV with the ATLAS detector. Eur. Phys. J. C **81**(2), 178 (2021). https://doi.org/10.1140/epjc/s10052-020-08677-2. arXiv:2007.02873 [hep-ex]
51. M. Aaboud et al., Search for the Higgs boson produced in association with a vector boson and decaying into two spin-zero particles in the $H \to aa \to 4b$ channel in pp collisions at $\sqrt{s} = 13$ TeV with the ATLAS detector. JHEP **10**, 031 (2018). https://doi.org/10.1007/JHEP10(2018)031. arXiv:1806.07355 [hep-ex]
52. A. Hayrapetyan et al., Study of WH production through vector boson scattering and extraction of the relative sign of the W and Z couplings to the Higgs boson in proton–proton collisions at $\sqrt{s} =$ 13 TeV. (2024). arXiv:2405.16566 [hep-ex]
53. M. Cacciari, G.P. Salam, G. Soyez, The anti-k_t jet clustering algorithm. JHEP **04**, 063 (2008). https://doi.org/10.1088/1126-6708/2008/04/063. arXiv:0802.1189 [hep-ph]
54. A. Babaev, CMS luminosity-public results. https://twiki.cern.ch/twiki/bin/view/CMSPublic/LumiPublicResults
55. D. Florian et al., Handbook of LHC Higgs cross sections: 4. Deciphering the nature of the Higgs sector. **2/2017** (2016). https://doi.org/10.23731/CYRM-2017-002. arXiv:1610.07922 [hep-ph]